Activity of perovskite La$_{1-x}$Sr$_x$MnO$_3$ catalysts towards oxygen reduction in alkaline electrolytes

John Tulloch, Scott W. Donne*

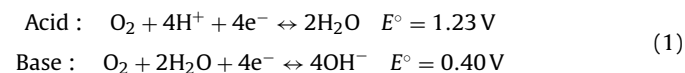*Discipline of Chemistry, University of Newcastle, Callaghan, NSW 2308, Australia*

ARTICLE INFO

ABSTRACT

The behaviour of the perovskite-based series of compounds La$_{1-x}$Sr$_x$MnO$_3$ (where x = 0, 0.2, 0.4, 0.6, 0.8 and 1.0) towards oxygen reduction in an ambient temperature alkaline 1 M KOH electrolyte is presented. Within this series, the intermediate compound La$_{0.4}$Sr$_{0.6}$MnO$_3$ exhibits the greatest catalytic activity, approaching that of the considerably more expensive fuel cell grade Pt-black examined under the same conditions. The origin of this activity is discussed in terms of material structure and morphology, which exists in the structural transition region between cubic LaMnO$_3$ and hexagonal SrMnO$_3$. The small crystallite size and relatively large BET surface area of this material reflect this high level of structural disorder. Furthermore, these features enable this compound to exhibit the greatest proportion of direct four-electron oxygen reduction (preferred) compared to the less efficient two-electron reduction to peroxide.

© 2009 Published by Elsevier B.V.

1. Introduction

It is generally accepted by the current scientific community that increasing levels of CO$_2$ and other greenhouse gases are contributing significantly to climate change. The major contributor to CO$_2$ levels is the combustion of fossil fuels in both industrial and transportation applications. Although research and development has provided some practical relief in the form of hybrid electric vehicles, their appearance on the roads and impact is far outweighed by the number of gasoline-powered vehicles.

Fuel cells are an excellent alternative to internal combustion engines, particularly because of their high specific energy, albeit at a relatively low power density [1]. Numerous types of fuel cell have been developed, each with their own distinctive mechanical properties and preferred working conditions. Examples include the proton-exchange membrane (PEM) fuel cell, the direct methanol fuel cell (DMFC), and the solid oxide fuel cell (SOFC). Irrespective of the type of fuel cell used, the cathodic reaction employed is always the catalytic reduction of oxygen, *i.e.*,

$$\begin{aligned} \text{Acid}: \quad & O_2 + 4H^+ + 4e^- \leftrightarrow 2H_2O \quad E^\circ = 1.23\,\text{V} \\ \text{Base}: \quad & O_2 + 2H_2O + 4e^- \leftrightarrow 4OH^- \quad E^\circ = 0.40\,\text{V} \end{aligned} \quad (1)$$

Traditionally, the catalyst used is platinum, which is attributable to its unquestionable catalytic performance and relatively low over-

potential [2]. Many different studies have been undertaken in an attempt to manufacture Pt-based materials as cathode catalysts which are cheaper than pure platinum, but their cost is still disadvantageous for large-scale implementation [3].

A class of materials known to show considerable catalytic activity are those based on the perovskite structure [4]. Advances in perovskite-type materials have shown that they possess mixed ionic and electronic conductivity, which is beneficial for catalytic activity [5]. In the case of fuel cells, where some inroads have been made into the use of perovskites, the catalyst must perform flawlessly as the oxygen reduction reaction is nearly 100 times slower than most anodic reactions [6,7], *e.g.*, H$_2$ oxidation. This is a fundamental limitation that many of the low-to-midrange temperature fuel cells encounter, and is primarily responsible for their limited power output [6].

In the past 10 years, considerable attention has been paid to perovskite materials falling within the classification La$_{1-x}$Sr$_x$MO$_3$ (where M is a transition metal) as catalysts for oxygen reduction. Two recently studied material series are those where M = Co (LSC) and Fe (LSF) [5,8–12]. The LSC materials show considerable oxide ion conductivity and sufficient electronic conductivity to make them of interest as mixed ionic-electronic conductors [5]. Additional catalysis work on the LSC series has shown that oxygen reduction may be limited by surface chemical exchange and solid-state diffusion, rather than the commonly accepted view that the electrode reactions are charge-transfer limited [5,11]. Another series of materials falling within this classification are those where M = Mn (LSM). These have been shown previously to have high electronic conductivity, as well as desirable thermal expansion and

* Corresponding author. Tel.: +61 2 4921 5477; fax: +61 2 4921 5472.
  E-mail address: scott.donne@newcastle.edu.au (S.W. Donne).

stability properties. Similar to the LSC series, their oxygen ion conductivities are quite low and therefore for it to function effectively the phase boundary between the electrolyte, the oxidizing gas and the catalyst-coated electrode needs to be maximized [13]. This communication describes work focused on examining the catalytic activity of the LSM series towards oxygen reduction in an alkaline environment.

2. Experimental

2.1. $La_{1-x}Sr_xMnO_3$ synthesis

Samples within this series were prepared thermally after the precursors had been mixed intimately using co-precipitation. Lanthanum(III), strontium(II) and manganese(II) acetates (>99.9% purity; Sigma–Aldrich) were first dried in air at 180 °C to remove the often variable water of crystallization from the starting materials. Appropriate amounts of these anhydrous acetates were then weighed out so as to obtain the correct stoichiometry, i.e., a 1:1 mole ratio of $La_{1-x}Sr_x$:Mn, where $x = 0, 0.2, 0.4, 0.6, 0.8$ and 1.0, and then dissolved into Milli-Q ultra-pure water. The resulting solution was stirred vigorously whilst being heated so as to remove the water fast enough such that the different acetates within the mixture precipitated essentially simultaneously, and not according to their relative solubilities. The co-precipitated acetate mixture was dried at 110 °C overnight, and then ground further using a mortar and pestle to enhance mixing of the precursors. This mixture was die-pressed (16 mm diameter) under 12 t to form a pellet, which was then sintered in air at 950 °C for 72 h. After this time period, the resultant material was allowed to cool slowly in the furnace, before being re-ground to make a loosely flowing powder.

2.2. Structural analysis

The structure of each LSM catalyst was examined by means of powder X-ray diffraction (XRD). A Philips X'Pert MPD system equipped with a Cu anode to generate Cu Kα radiation (1.5418 Å) was used. Each diffraction pattern was recorded in the 2θ range of 10–90°, with an equivalent 2θ step size of 0.008° and a count time of 45 s.

2.3. BET surface area

0.1 g of each catalyst material was degassed under vacuum at 110 °C for 2 h. The sample was than allowed to cool to room temperature, reweighed to determine the dry weight of catalyst, and then attached to a Micromeritics ASAP 2020 Surface Area Analyzer. An adsorption isotherm was then collected in the partial pressure (P/P_0) range of 0.05–0.30 using N_2 as the adsorbate at 77 K. The surface area was calculated from the adsorption data according to the BET isotherm [14].

2.4. Conductivity measurements

The conductivity of each catalyst material was determined by compacting the sample between two Au-coated stainless-steel pistons (1.3 cm diameter) in an insulating, ceramic-lined, steel-reinforced tube under a pressure of 5 t for 2 min using a hydraulic press. While under this compaction pressure, an insulated steel frame was screwed into position around the long axis of the pistons to ensure a constant pressure on the sample when removed from the hydraulic press. When removed from the press, the resistance (R, Ω) of the compacted pellet was measured after a 24 h equilibration at individual temperatures ranging from ambient up to 100 °C using a Keithley Instruments multimeter. The conductivity (σ, S cm^{-1}) was then determined using the expression:

$$\frac{1}{\sigma} = \rho = R\frac{l}{A} \tag{2}$$

where ρ is the resistivity (Ω cm), and l and A are the pellet thickness (cm) and cross-sectional area (cm^2), respectively. From the conductivity as a function of temperature, and activation energy for conduction (E_A, kJ mol^{-1}) was determined assuming Arrhenius behaviour.

2.5. Electrochemical characterization

The activity of each catalyst was evaluated using a rotating ring-disc electrode (RRDE; AFE6M shaft with a AFE6R1PT tip, Pine Instrument Company) that consisted of a hands-off, removable 5 mm diameter glassy carbon (GC) disc (ACE6DC050GC) and a Pt ring (6.5 mm i.d. and 7.5 mm o.d.).

2.5.1. Glassy carbon electrode preparation

To attain a true representation of individual catalyst performance, steps had to be taken to ensure that the GC disc electrode had no 'history' from previous tests, and that it was hydrophilic so that the catalyst ink would completely wet the GC surface and form a uniform catalyst layer. As such, the GC electrode was allowed to soak in a solution of 0.1 M H_2SO_4/0.1 M H_2O_2 for a 12-h period prior to catalyst deposition. This solution has the ability to solubilize transition metal oxides, which effectively cleans the surface. Next, the GC electrode was rinsed with Milli-Q ultra-pure water before being dried in air at 50 °C.

2.5.2. Ink preparation

To mount the catalyst materials on the GC disc electrode, they were first ground into a fine free-flowing powder using an agate mortar and pestle (~10 min). A 25 mg sub-sample was then taken and suspended in 25 mL of Milli-Q ultra-pure water that had been dosed with 250 μL of Nafion® 117 solution (Fluka). The resulting suspension was ultrasonicated for 30 min before a 20 μL sample was taken and dropped on the GC electrode surface, which was allowed to dry in air. This led to an average catalyst loading of 21.3 ± 0.4 μg on the GC electrode surface.

2.5.3. Electrochemical protocol

The electrolyte used throughout the work was an aqueous solution of 1.0 M KOH, prepared from pelletized KOH of the highest purity (Sigma–Aldrich) and O_2-saturated Milli-Q ultra-pure water. After preparation, the electrolyte was stored under O_2 in a sealed vessel to prevent CO_2 dissolution. Prior to electrochemical experimentation, the electrolyte was purged in the electrochemical cell with a stream of wet O_2 for at least 1 h to achieve saturation. During the purging process, the fully assembled RRDE electrode was immersed in the electrolyte together with a Hg|HgO (1 M KOH) reference electrode and a Pt foil (4 cm^2) counter electrode. This was to allow full wetting of the catalyst surface prior to conducting the electrochemical experiment. After being fully purged, the gas stream was removed from the electrolyte, but left in the electrochemical cell to form a blanket of O_2 over the electrolyte. At that point, rotation of the RRDE was initiated using a modulated speed rotator (Pine; AFMSRCE). The RRDE was allowed to rotate at open circuit for ~5 min to equilibrate. Rotation rates of 100–2000 rpm were used. The reduction of O_2 on each catalyst was then carried out by sweeping the electrode voltage from +0.4 to −1.0 V at 5 mV s^{-1} using a Pine Instrument Company AFCBP1E bipotentiostat controlled by PineChem software.

3. Results and discussion

3.1. Structural analysis

Fig. 1 shows the XRD patterns for the series of $La_{1-x}Sr_xMnO_3$ compounds synthesized in this work. The first point to note about the compounds is that they are relatively phase pure, with the patterns showing no evidence of the expected impurities Mn_2O_3/Mn_3O_4, La_2O_3 or SrO. Miller indicies for the parent material $LaMnO_3$, based on a cubic unit cell, have also been included in Fig. 1. As the mole fraction of strontium is increased, there is a progressive loss of symmetry, *i.e.*, a shift from cubic $LaMnO_3$ to hexagonal $SrMnO_3$, despite the fact that perovskites are generally classified as cubic materials. The cause of this is the change in manganese oxidation state from 3+ when $x = 0$, to 4+ when $x = 1$. Mn^{3+} is a Jahn–Teller distorted transition metal forming an elongated axial octahedron, which in this case has lowered the unit cell symmetry.

From the XRD patterns in Fig. 1, it was possible to calculate unit cell dimensions for each compound in the series assuming both (pseudo) cubic and hexagonal unit cell dimensions. Fig. 2 (and also Table 1) shows the changes in unit cell volume for both types of unit cell. Clearly, the unit cell volume decreases as the strontium mole fraction increases, or in other words as the manganese oxidation state transitions from 3+ to 4+. This is consistent with the fact that the ionic radius of Mn^{4+} (67 pm) is smaller than that of Mn^{3+} (79 pm), and indicates that the manganese ionic radius is in fact the determinant of the unit cell size. This is significant since La^{3+} (117 pm) has a smaller ionic radius compared with Sr^{2+} (132 pm) [15].

The XRD patterns, via application of the Scherrer equation [16] to selected peaks, have also been used to determine the primary par-
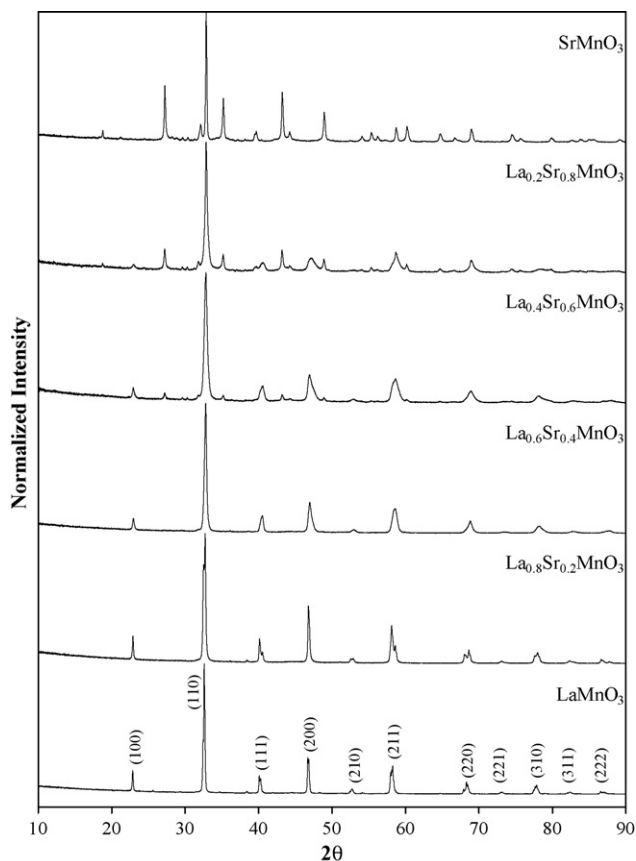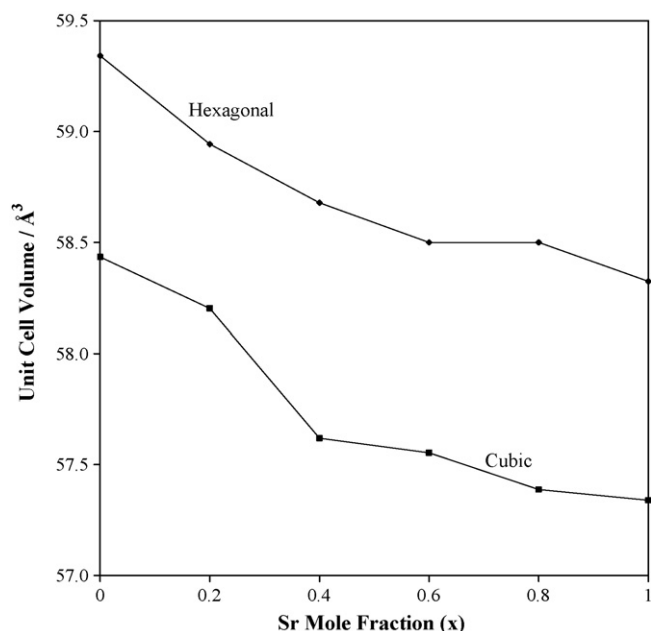

Fig. 2. Unit cell volume for $La_{1-x}Sr_xMnO_3$ series of compounds.

ticle size of each compound; the calculated values also are included in Table 1. There is apparently a minimum in crystallite size at $La_{0.4}Sr_{0.6}MnO_3$ which may very well represent the structural transition of this series of compounds from cubic $LaMnO_3$ to hexagonal $SrMnO_3$, with the greatest disorder in the structure occurring at or near to this composition. Starting with cubic $LaMnO_3$, replacing some of the La^{3+} with Sr^{2+} leads to the formation of a solid solution in which the Sr^{2+} is distributed randomly over the entire structure. Therefore, there is the potential for atomic-scale localized regions of hexagonal symmetry within the structure associated with the Sr^{2+} ions. With the addition of Sr^{2+}, however, the manganese oxidation state is expected to change proportionately from Mn^{3+} to Mn^{4+}. The impact of this change in oxidation state is potentially more serious for the structure, because as has been demonstrated previously, it is the manganese oxidation state that dictates the size of the unit cell. The electron associated with Mn^{3+}/Mn^{4+} species can be either mobile or localized with the Sr^{2+} in the structure. Given the substantial conductivity of this series of compounds (shown in Table 1 and to be discussed later), it would be reasonable to assume that the electron is actually quite mobile. By contrast, the rather large La^{3+} and Sr^{2+} ionic species are expected to be quite immobile, at least at ambient temperature. With such a relatively mobile electron, it is expected that the effects of manganese oxidation state (in particular Jahn–Teller distortion) will be dispersed over the entire structure (cooperative distortion) rather than be localized. As such, structural strain introduced as a result of this compositional transition should be minimized. This is somewhat contrary to the crystallite size data that have been calculated from the XRD data. With a minimum observed in the crystallite size, it may be concluded that this corresponds to a maximum in structural strain possibly as a result of charge localization within the structure. Assuming that the electronic charge is actually localized within the structure, as the Sr^{2+} content increases, so too is the structural strain at the boundary between the newly formed hexagonal domains. With more strain present, the ability of the structure to maintain extended crystallinity is diminished, and as such so is the crystallite (or primary particle) size. When sufficient Sr^{2+} has been added so that the hexagonal domains predominate, structural strain diminishes allowing for larger crystallite sizes. Since there are substantial changes in crystallite size over the composi-

Fig. 1. X-ray diffraction patterns for series of compounds $La_{1-x}Sr_xMnO_3$ where $0 \leq x \leq 1$.

Table 1
Selected characterization data for La$_{1-x}$Sr$_x$MnO$_3$ catalysts.

Compound	a_0 (Å)[a]	Unit cell volume (Å^3)[a]	Crystallite size (nm)	BET SA (m^2 g^{-1})	σ (S cm^{-1})[b]	E_A (kJ mol^{-1})	$\lvert i_{max} \rvert$ (mA cm^{-2})[c]	H$_2$O$_2$ formation (%)[d]
LaMnO$_3$	3.8805	58.43	143	2.6	0.065	20.6	1.16	81 ± 2
La$_{0.8}$Sr$_{0.2}$MnO$_3$	3.8754	58.20	86	4.2	0.039	22.4	1.47	37 ± 2
La$_{0.6}$Sr$_{0.4}$MnO$_3$	3.8624	57.62	65	9.6	0.007	22.5	1.52	32 ± 2
La$_{0.4}$Sr$_{0.6}$MnO$_3$	3.8609	57.55	47	6.2	0.099	17.2	1.77	15 ± 2
La$_{0.2}$Sr$_{0.8}$MnO$_3$	3.8572	57.39	50	2.5	0.109	17.7	1.37	37 ± 2
SrMnO$_3$	3.8561	57.34	91	1.7	0.284	13.4	1.05	74 ± 2

[a] Assuming pseudo-cubic unit cell geometry.
[b] Measured at 22 °C.
[c] Corresponds to data in Fig. 3 (500 rpm).
[d] Corresponds to rotation rate of 500 rpm.

tional range, it is concluded that charge localization does indeed predominate.

3.2. Morphological and conductivity analysis

The morphology of each sample was characterized in terms of BET surface area, which in effect represents the porosity of the material. Given that the materials were prepared thermally at a high temperature for a prolonged period of time, they are expected to be quite crystalline with low surface areas (<1 m^2 g^{-1}). The BET surface area data (Table 1) indicates, however, that in some instances a high degree of porosity has been retained. Significantly, there appears to be an inverse relationship between crystallite size and BET surface area, i.e., samples with small crystallite size have relatively larger BET surface areas. In some ways, this is understandable given the preceding observation that induced strain in the structure decreases the crystallite size and thereby promotes the formation of pores between these smaller crystallites. The fact that the samples retain such a relatively high degree of crystallinity is notable because during catalytic action an increased interfacial area is beneficial with respect to performance.

Suitable conductivity within the catalyst is of course required for optimum performance since, for catalysed redox reactions, the substrate has to act as a source or sink of electrons. For the series of compounds prepared in this work, the conductivities of the compacted pellets at 22 °C have also been included in Table 1. The data indicate that the compounds are indeed semiconductors, with moderate conductivity ranging from 0.007 to 0.284 S cm^{-1}, which is considered to be sufficient for catalytic action. Furthermore, there appears to be a trend in the data whereby as the Sr^{2+} level in La$_{1-x}$Sr$_x$MnO$_3$ is increased the conductivity initially drops, but then after a composition of La$_{0.6}$Sr$_{0.4}$MnO$_3$ adding more Sr^{2+} increases the conductivity. The increase in conductivity while approaching the composition SrMnO$_3$ is to be expected given that there is also a progressive increase in the average manganese oxidation state, in which case there is substantial literature to indicate that Mn^{4+} compounds are more conductive than those containing Mn^{3+} [17]. The origin of the slight decrease in conductivity at low Sr^{2+} contents is not apparent at this time; it may, however, be due to charge ordering within the structure.

An interesting observation concerning the conductivity data reported in Table 1, one that may influence the interpretation of the data, is that the conductivity appears to be proportional to the crystallite size and inversely proportional to the BET surface area. It is important to recognize at this point that these conductivity values contain contributions from both the intrinsic conductivity (σ_i) of the solid state, as well as that of the grain boundaries (σ_{gb}), i.e.,

$$\frac{1}{\sigma} = \frac{1}{\sigma_i} + \frac{1}{\sigma_{gb}} \tag{3}$$

While an attempt was made in this work to minimize the contribution made by grain boundaries by compacting the powders under

relatively high pressures to form the pellet on which measurements were made, it is not possible to remove it completely. By using a high compaction pressure, grain boundaries are forced together in an attempt to have the grain boundary mimic the bulk structure. Clearly, this will only be achieved at the highest of pressures where the actual movement of ions is induced. The most acceptable "artificial" way to achieve this is by sintering the compacted powder; however, this is inappropriate in this instance because it will alter the microstructure of the materials. Therefore, any conclusions based on the conductivity data presented in Table 1 must be tempered by the fact that the values may be influenced by the microstructure of the material. In any case, the main point is that the materials are indeed conductive and can function as sources and sinks for electrons.

3.3. Electrochemical characterization

Before proceeding to analyse and discuss the electrochemical data collected in this study, it is appropriate to describe some of the details associated with the oxygen reduction reaction. The general mechanism by which oxygen is reduced in an aqueous media is as shown in Eq. (4), where k_i represents the rate constant for the various processes [18].

$$\tag{4}$$
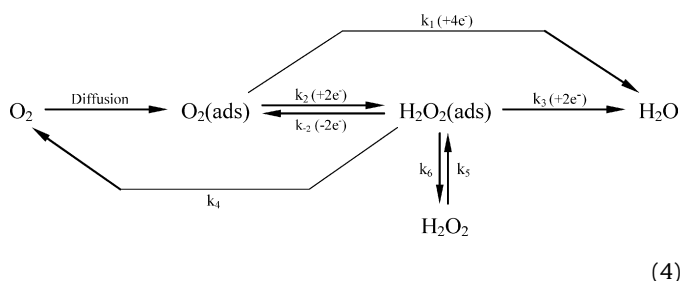
There are two competing reaction mechanisms with different rate constants (k_1 and k_2 with subsequent steps). The reaction characterized by k_1 is the direct four-electron reduction of adsorbed oxygen in the presence of protons to form water. This pathway does not create any reaction intermediates and is known to be the most efficient reaction mechanism [18]. The competing mechanism characterized by k_2 is the indirect two-electron reduction of adsorbed oxygen and proceeds via the intermediates H$_2$O$_2$(ads) and H$_2$O$_2$. This incomplete reduction to the peroxide intermediate not only leads to low energy-conversion efficiency, but also generates the chemically aggressive peroxide species that can further convert into harmful radical species. The peroxide formed in the two-electron mechanism is severely detrimental to the range of compounds examined here, as most manganese compounds with a high oxidation state are susceptible to reduction (to form soluble Mn^{2+}) by the peroxide [19]. It has been found that the amount of peroxide intermediate produced in alkaline media is greater than that in acidic media [20,21]. In alkaline solutions, as little as 60%
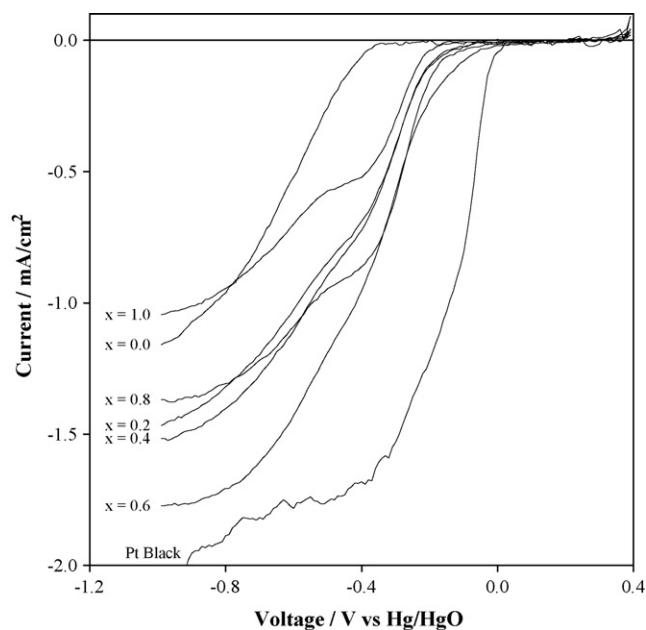
Fig. 3. Measured disc current for $La_{1-x}Sr_xMnO_3$ catalysts compared with fuel cell grade Pt black (500 rpm).

Fig. 4. Measured disc current for $La_{0.6}Sr_{0.4}MnO_3$ catalyst as function of rotation rate. Values attached to curves are rotation rates in rpm.

of the reduction current is associated with the direct reduction mechanism with the remainder contributing to the formation of the peroxide intermediate, and thereby suggests a much more complicated reaction mechanism [22]. On the other hand, the activity for oxygen reduction reaction has been observed to be higher in alkaline rather than in various acidic media, probably due to the minimal specific adsorption of the OH^- ion [22].

To begin the comparison between the various catalysts prepared in this work, Fig. 3 presents an RDE voltammogram for each of the catalysts (500 rpm). For comparison, the behaviour under the same conditions of fuel cell grade Pt-black is also included. The data have been normalized with respect to the area of the GC electrode. The first feature to discuss is the shape of the voltammograms. For a single-step reduction process, a straightforward sigmoidal current response as a function of voltage should be observed. In almost all instances, however, the current response contains a combination (to varying extents) of two sigmoidal curves. This is almost certainly due to the parallel occurrence of two- and four-electron oxygen reduction processes.

The next comment that needs to be made concerns the maximum current achieved for each of the catalysts. Diffusion-limited oxygen reduction conditions are attained at suitably low voltages, in which case, given that the oxygen concentration in the 1.0 M KOH was the same for all experiments, the same current for each catalyst should have been achieved. Clearly, this is not the case, but, it is interesting to note that the maximum current parallels somewhat the BET surface area of the individual catalysts (Table 1). This suggests that the porous structure of the catalyst is playing a role in the catalytic activity, even during the RDE experiment. If the current is normalized according to the BET surface area, then the voltametric data at low voltages does indeed cluster together (0.4 ± 0.1 mA cm^{-2}/(m^2 g^{-1})), with any apparent differences due perhaps to the pore-size distribution of the catalyst.

A typical example of the effects of rotation rate on catalytic activity is shown in Fig. 4, in this instance for the $La_{0.6}Sr_{0.4}MnO_3$ catalyst. As expected, the current flowing increases as the diffusion layer is made thinner at higher rotation rates. Analysis of the data for all catalysts is undertaken through use of the Koutecky–Levich expression
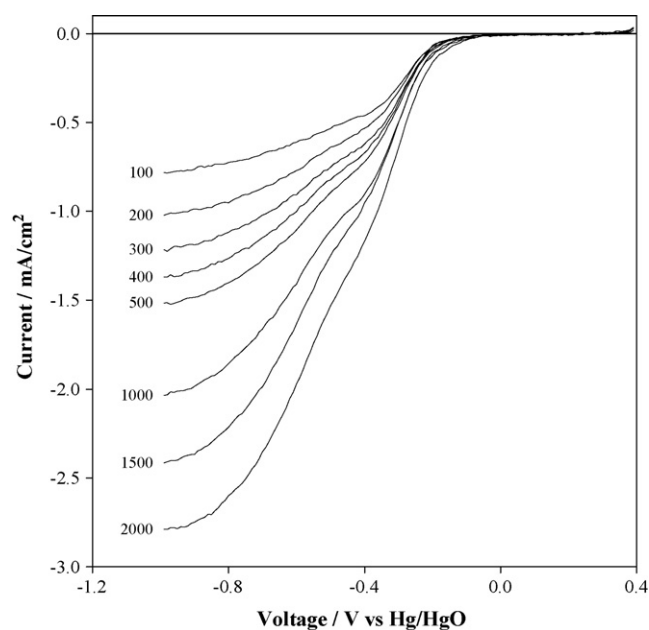
[23], *i.e.*,

$$\frac{1}{i} = \frac{1}{i_k} + \frac{1}{i_d} = \frac{1}{i_k} + \frac{1}{0.620nFAC_{O_2}(D_{O_2})^{2/3}\nu^{-1/6}\omega^{1/2}} \tag{5}$$

where i_k is the kinetic current, i_d the diffusion-limited current, ν the kinematic viscosity, ω is the angular frequency, and all other symbols have their usual electrochemical significance. From Eq. (5), a plot of i^{-1} vs. $\omega^{-1/2}$ should give a straight line for which the Y-intercept is i_k^{-1} and hence i_k can be easily extracted. Additionally, if needed, the slope of such a plot can be related back to the diffusional properties of the oxygen. The slopes of the data sets given in Fig. 5 are essentially the same and therefore indicate consistent diffusional characteristics in the system.
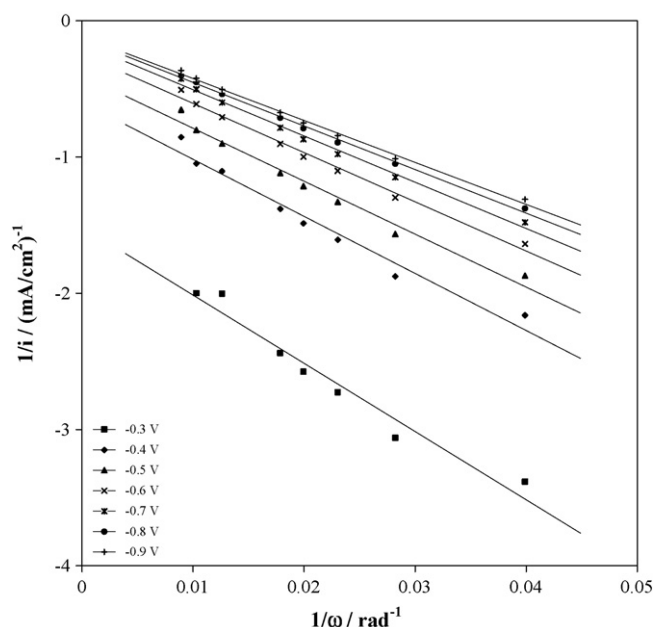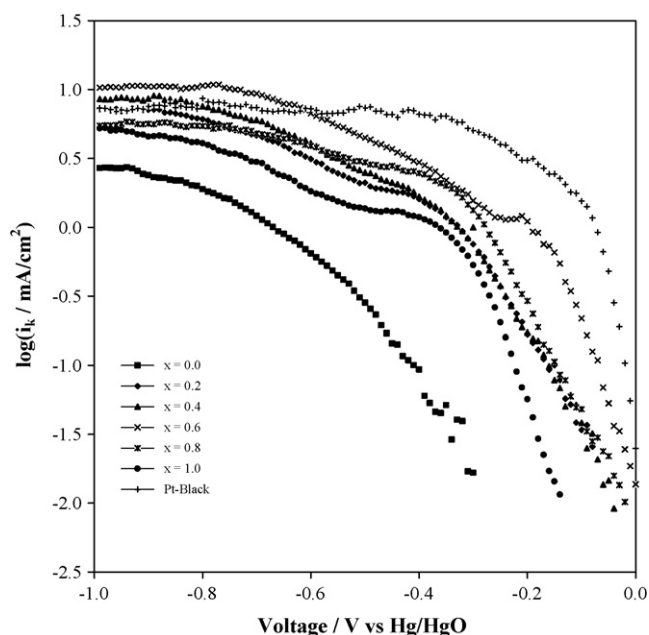

Fig. 5. Sample Koutecky–Levich plot for $La_{0.6}Sr_{0.4}MnO_3$.

Fig. 6. Tafel plot for each $La_{1-x}Sr_xMnO_3$ catalyst compared with that of fuel cell grade Pt-black.

At this point, it is now possible to compare the catalytic performance of each compound by generating a Tafel plot ($\log(i_k)$ vs. V), as shown in Fig. 6. The results demonstrate that fuel cell grade Pt black is indeed the preferred catalyst; it outperforms all of the $La_{1-x}Sr_xMnO_3$ catalyst materials, except at low voltages (high overpotentials) where the catalyst $La_{0.4}Sr_{0.6}MnO_3$ gives a greater catalytic current. Nevertheless, given the relative costs of platinum compared with lanthanum, strontium and manganese, and the fact that the best-performing perovskite catalyst ($La_{0.4}Sr_{0.6}MnO_3$) had at most a 0.15 V greater overpotential, there is the possibility that this catalyst could be a viable alternative. Within the domain of $La_{1-x}Sr_xMnO_3$ catalysts, it is also clear that the compound with $x = 0.6$ is the optimum, with compositions on either side of this value falling off in terms of performance. The underlying reasons why this composition yields the best performance are unknown at this stage. From a morphological standpoint, however, this material has the smallest crystallite size and a relatively large BET surface area, which does imply that such material properties can have an impact on performance.

The performance of a catalyst depends on the way in which the catalyst associates with molecular oxygen during the initial stages of the reduction process. A strong association infers that the catalyst surface may be poisoned by the formation of an oxide layer, while a weak association may lead to poor activation of the charge-transfer process [24]. Quantitatively, the desired oxygen adsorption energy on to the catalyst substrate is unknown, but intermediate adsorption energies are desired. The crystal structure of the catalyst can affect the adsorption energy because the oxygen molecule has to bind effectively with the catalyst surface [24]. Given the structural data presented in Table 1, which does not show a minimum but rather a progressively decreasing unit-cell size, the relationship between crystal structure and the strength of oxygen adsorption is not straightforward.

A feature of perovskite-based compounds that, in general, has an effect on their catalytic ability is the level of defects within the structure [25]. It has been noted above that the best-performing catalyst has the smallest crystallite size, which is suggests that it possesses a relatively defective structure. The defects may be induced as a result of the structural transition from cubic $LaMnO_3$ to hexagonal $SrMnO_3$, with the inherent structural strain at this transition point leading to a more defective structure. The nature of the defects, if these are indeed present, is likely to be associated with lattice dislocations in going from one structure to the other. Whatever the origin of the defects, they apparently induce a higher activity in the catalyst substrate.

3.4. Peroxide formation

In the cathode compartment of a fuel cell, it is highly desirable to avoid the formation of a peroxide species because of the lower energy-conversion efficiency of the two-electron reduction, and also because peroxide is chemically aggressive towards the catalyst. The latter feature leads to reduction of the catalyst (to either Mn_3O_4 or $Mn(OH)_2$ in an alkaline environment [26]), and hence loss of catalytic activity. To measure peroxide formation for the catalysts studied here, the optimum collection efficiency of the RRDE system was first determined by using a solution of $Fe(CN)_6^{3-}$ in 1 M KCl, which is regarded as a model system. The voltage of the disc electrode was cycled between 0.8 and −0.1 V vs. a saturated calomel electrode (SCE), while the ring potential was set at 0.7 V vs. SCE to re-oxidize any reduction product ($Fe(CN)_6^{4-}$) that made its way to the ring after being formed on the disc. The collection efficiency (N) is defined by [23]:

$$N = \frac{-i_R}{i_D} \tag{6}$$

where i_R and i_D are the respective ring and disc currents flowing at the same voltage. For the $Fe(CN)_6^{3-}$ active species in 1 M KCl, the collection efficiency of the electrode varied over the range of 24.4–25.3%, with the slower rotation rates leading to a more efficient collection. After this electrode calibration, catalyst-loaded electrodes were placed in a O_2-saturated 1 M KOH electrolyte, and the disc voltage scanned at 5 mV s^{-1} from 0.4 to −1.0 V vs. Hg|HgO, as used previously. The ring potential was held at 0.2 V vs. the Hg|HgO, which is a suitable potential to cause mass-transfer limited oxidation of any peroxide formed, but not to decompose water. A typical example of the results is shown in Fig. 7, in this case for $La_{0.2}Sr_{0.8}MnO_3$ rotated at 500 rpm. Notably, although there are two reduction waves, only one wave (at higher voltages) is observed in the ring current data. This type of behaviour is shown by a number of the catalysts (see Fig. 3), and is indicative of the poor activity of some of the catalysts towards the four-electron reduction of oxygen, giving preference to two-electron reduction at high voltages. The RRDE data also indicates that there is indeed a competition between the four- and two-electron reduction processes, with the more active catalysts having a lower overpotential for the four-electron reduction.

The collection efficiency for each of the catalyst-loaded electrodes was determined via Eq. (6) and then expressed as a percentage of the $Fe(CN)_6^{3-}$/1 M KCl system collection efficiency under the same conditions so as to provide a quantitative indication of the amount of charge going to peroxide formation. These values are included in Table 1 for a rotation rate of 500 rpm was used. There is a clear minimum in the amount of peroxide formation (at $15 \pm 2\%$) when $La_{0.4}Sr_{0.6}MnO_3$ is used. Fuel cell grade Pt-black under the same conditions reported $12 \pm 2\%$ of the total charge going to peroxide formation, which, within experimental error, is comparable with the performance of the aforementioned catalyst. Interestingly, if the maximum current flowing due to oxygen reduction is compared with the percentage of charge going to peroxide formation (Table 1), a good inverse correlation is observed, as shown in Fig. 8. This indicates that the direct four-electron reduction of oxygen is overall more facile than the two-electron reduction to peroxide, and that the catalyst $La_{0.4}Sr_{0.6}MnO_3$ is the best material for facilitating four-electron reduction. Morphologically this material has the smallest crystallite size and one of the largest active surface
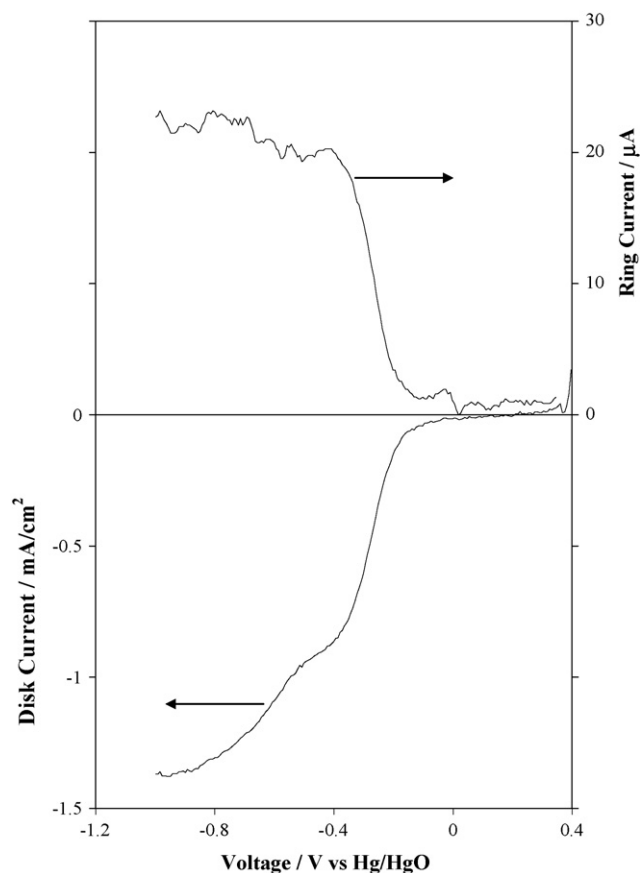
Fig. 7. Sample ring and disc currents from RRDE experiment with $La_{0.2}Sr_{0.8}MnO_3$ rotated at 500 rpm.

areas but these reasons alone do not explain the preference of the four- compared with two-electron reduction mechanism. Investigations to explain this behaviour will be the subject of a future communication.
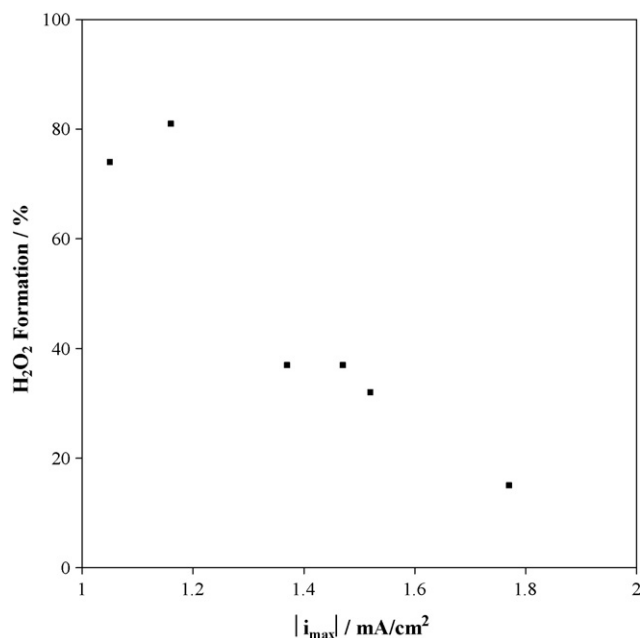

Fig. 8. Relationship between maximum current achieved and amount of peroxide generated on each catalyst.

4. Summary and conclusion

A range of techniques have been used to examine the physical and electrochemical properties of the perovskite-based compounds $La_{1-x}Sr_xMnO_3$ ($x = 0$, 0.2, 0.4, 0.6 0.8 and 1.0) towards oxygen reduction in aqueous alkaline media (1 M KOH). The following summarizes the key findings.

(i) Phase-pure compounds within the series are prepared by co-precipitation of precursor acetates to form an intimate mixture that is pelletized and then heat-treated at 950 °C for 72 h. These conditions are sufficient to allow inter-diffusion of the precursors, as well as crystallization of the resultant structure.

(ii) The parent compound within the series ($LaMnO_3$) undergoes structural transition from pseudo-cubic to hexagonal geometry as the strontium content is increased. Furthermore, the unit-cell size shrinks with this transition. This observation is indicates that the manganese oxidation state determines the unit-cell size rather than the lanthanum/strontium ionic mixture, *i.e.*, the ionic radii of the Mn(III/IV) couple in $LaMnO_3/SrMnO_3$ (79 pm vs. 67 pm) match the observed trend compared with the ionic radii of La(III) and Sr(II) (117 pm vs. 132 pm, respectively).

(iii) Perhaps due to induced strain as a result of the structural transition, a minimum in crystallite size and a maximum in BET surface area are observed at intermediate compositions throughout the series. Most often this coincides with the compound $La_{0.4}Sr_{0.6}MnO_3$.

(iv) Electrochemically, the compound $La_{0.4}Sr_{0.6}MnO_3$ also exhibits the best performance with the highest catalytic activity towards oxygen reduction, most of which is due to the preferred direct four-electron reduction, rather than the parasitic two-electron reduction to peroxide. An attempt has been made to explain the link between catalyst composition and performance in terms of the morphological properties of the catalysts, but a greater understanding of the preferred catalyst surface and its interaction with adsorbed oxygen is needed. Overall, the performance of the best compound in this series is still inferior to that of fuel cell grade Pt-black. Nevertheless, this limitation may be acceptable given the much lower cost of perovskite-based catalysts.

References

[1] T. Christen, M.W. Carlen, J. Power Sources 91 (2000) 210.
[2] S. Gottesfeld, ECS Trans. 6 (25) (2008) 51.
[3] N.N. Markovic, T.J. Schmidt, V. Stamenkovic, P.N. Ross, Fuel Cells 1 (2001) 105.
[4] L.G. Tejuca, J.L.G. Fierro, J.M.D. Tascon, Adv. Catal. 36 (1998) 237.
[5] S.J. Skinner, Int. J. Inorg. Mater. 3 (2001) 113.
[6] T. Jacob, Fuel Cells 6 (2006) 159.
[7] S. Thomas, M. Zalbowitz, Fuel Cells – Green Power, Los Alamos, NM, USA, 2000.
[8] H.Y. Tu, Y. Takeda, N. Imanishi, O. Yamamoto, Solid State Ionics 100 (1997) 283.
[9] M. Godickemeier, K. Sasaki, L.J. Gaulkler, I. Reiss, J. Electrochem. Soc. 144 (1997) 1635.
[10] T. Kawada, K. Masuda, J. Suzuki, A. Kaimai, K. Kawamura, Y. Nigara, J. Mizusaki, H. Yugami, H. Arashi, N. Sakai, I. Yokokawa, Solid State Ionics 121 (1999) 271.
[11] S.B. Adler, Solid State Ionics 111 (1998) 125.
[12] R.H.E. van Doorn, A.J. Burggraaf, Solid State Ionics 128 (2000) 65.
[13] S.P.S. Badwal, S.P. Jiang, J. Love, J. Nowotny, M. Rekas, E.R. Vance, Ceram. Int. 27 (2001) 419.
[14] S. Brunauer, P.H. Emmett, E. Teller, J. Am. Chem. Soc. 60 (1938) 309.
[15] R.D. Shannon, C.T. Prewitt, Acta Crystallogr. B 25 (1969) 925.

[16] A.R. West, Solid State Chemistry and its Applications, John Wiley and Sons, 1984.
[17] X. Xia, H. Li, Z.-H. Chen, J. Electrochem. Soc. 136 (1989) 266.
[18] B. Wang, J. Power Sources 152 (2005) 1.
[19] S.W. Donne, unpublished results.
[20] K. Wiik, C.R. Schmidt, S. Faaland, S. Shamsili, M. Einarsrud, T. Grande, J. Am. Ceram. Soc. 82 (1999) 721.
[21] F.W. Poulsen, N. van der Puil, Solid State Ionics 53–56 (1992) 777.
[22] E.H. Yu, K. Scott, R.W. Reeve, Fuel Cells 3 (2003) 169.
[23] A.J. Bard, L.R. Faulkner, Electrochemical Methods: Fundamentals and Applications, John Wiley and Sons, 1980.
[24] V. Stamenkovic, J.K. Nørskov, et al., Angew. Chem. Int. Ed. 45 (2006) 2897.
[25] T. Tsai, S.A. Barnett, Proc. Electrochem. Soc. 97 (40) (1997) 368.
[26] M. Pourbaix, Atlas of Electrochemical Equilibria in Aqueous Solutions, 2nd edition, National Association of Corrosion Engineers, 1974.